Journal of Materials Chemistry A

Accepted Manuscript

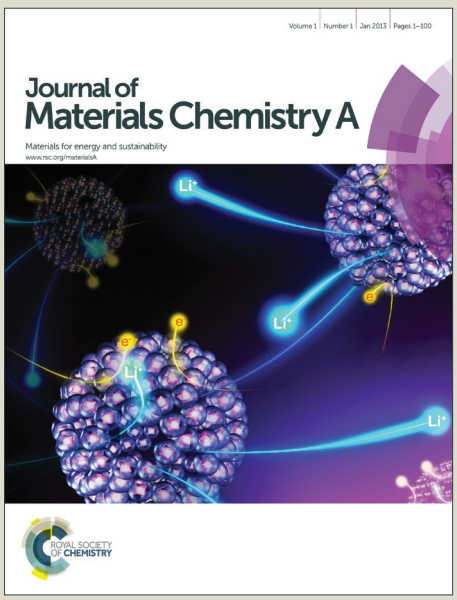

ROYAL SOCIETY OF CHEMISTRY

www.rsc.org/materialsA

Journal of Materials Chemistry A

ARTICLE

Oxygen evolution catalyst on antimony doped tin oxide nanowire structured support for proton exchange membrane liquid water electrolysis

Received 00th January 20xx,
Accepted 00th January 20xx

DOI: 10.1039/x0xx00000x

www.rsc.org/

Gaoyang Liu[a,b], Junyuan Xu[c], Yituo Wang[a,b] and Xindong Wang[a,b*]

Developing catalysts with high electrocatalytic activity has recently attracted much attention due to the slow reaction kinetics for oxygen evolution reaction (OER) and poor durability under harsh operating environments. Aiming at enhancement of oxygen electrode kinetics and durability, a facile and scalable electrospinning method is employed to fabricate antimony doped tin oxide nanowire (Sb-SnO_2 NW) as support materials for iridium oxide. Both the scanning electron microscope (SEM) and transmission electron microscope (TEM) results show that the as prepared Sb-SnO_2 NW is stacked from primary Sb-SnO_2 nanoparticles (Sb-SnO_2 NP) with diameters of 15-25 nm and exhibits uniform porous nanowire structure with diameter in the range of 200-300 nm. The synthesized Sb-SnO_2 NW has a BET surface area of 60 m^2 g^{-1} and an electronic conductivity of 0.83 S cm^{-1}. Benefiting from porous nanowire structure and high electronic conductivity of the Sb-SnO_2 NW support, the supported IrO_2 catalyst exhibits significant enhancement of mass activity toward OER in acidic electrolytes comparing with Sb-SnO_2 NP supported IrO_2 catalyst and pure IrO_2. The improved catalytic performance for OER is further confirmed by proton exchange membrane (PEM) electrolyzer tests at 80 °C. A test of such an electrolyzer cell at 450 mA cm^{-2} shows good durability within a period of up to 646 h.

Introduction

Renewable sources have been utilized via various methods for power generation, but not all the electricity is fed into the grid. Storage of the excess energy in the form of hydrogen is essential for the realization of large scale deployment of renewable sources. [1] The method to generate hydrogen is the key in hydrogen energy development. So far, water electrolysis is one of the most practical ways to produce pure hydrogen from renewable energy sources. Compared with the traditional alkaline electrolysis, proton exchange membrane (PEM) water electrolysis has been considered as the most promising system in the future due to its higher current densities, energy efficiency and purity of the hydrogen product. Especially for the PEM water electrolyser based on Nafion® membranes operated below 80 °C or room temperature, it has advantages for practicability, and little demanding for thermal management and the subsequent gas product compression operations.[2]

The high positive anode potential and the oxygen evolution in acid environment represent a very severe test for electrocatalysts. Only precious metal oxides are relatively stable. Typically, the currently used oxygen evolution reaction (OER) catalysts are based on IrO_2 and/or RuO_2.[3] The major challenge of OER catalysts research is to reduce (noble metal) investment cost, while offer fast kinetics and is stable in a harsh oxidising environment of low pH values and high electrode potentials.[4-5] One method to achieve this is to prepare composite oxide catalysts, i.e. iridium oxides doped with oxides of Sn[6], Ti[7], Si[8], Mn[9], Co[10], Ce+Nb[11], Ta[12] and Mo[13] metals. General speaking, these doping metal oxides could increase the active surface area by the mechanisms of the grain refinement,8,[13] pore morphology8, porosity[11] and surface enrichment of the active phase[18]. However, these doping metal oxides showed little beneficial effects other than serving as diluent matrices.7,[18] Besides, these doping metal oxides are electrochemically inert and poor electronic conductivity.[14] Excessive addition of the doping metal oxides in the composited oxide catalysts will dilute the IrO_2 and/or RuO_2 oxide content and lead to a decrease of the active area. As a result, the normalized catalytic activity of the composite oxide catalysts is low compared with that of catalysts made of pure IrO_2 and/or RuO_2, especially when the content of IrO_2 and/or RuO_2 is much lower than 60-80%.

To optimize the utilization of IrO_2 and/or RuO_2 and at the same time to improve the catalyst activity towards the OER, another effective approach is to disperse the noble metal

[a] State Key Laboratory of Advanced Metallurgy, University of Science and Technology Beijing, 30 College Road, Beijing 1 00083, China. E-mail: echem@ustb.edu.cn; Fax:+86 10 62332651; Tel: +86 10 62332651
[b] Department of Physical Chemistry, University of Science and Technology Beijing, 30 College Road, Beijing 100083, China. E -mail: echem@ustb.edu.cn; Fax: + 86 10 62332651; Tel: +86 10 62332651
[c] Shenyang National Laboratory for Materials Science, Institute of Metal Research, Chinese Academy of Science, 72 Wenhua Road, Shenyang 110016, China
† Footnotes relating to the title and/or authors should appear here.
Electronic Supplementary Information (ESI) available: [details of any supplementary information available should be included here]. See DOI: 10.1039/x0xx00000x

active phase on high surface area non-noble supports.[15] In essence, both of the doping metal oxides and the supports are used to increase the active surface area and then improve the apparent reaction rate. While, an obvious advantage of using a support comparing with the doping metal oxides is that the morphology of the support can be tailored to achieve higher degree of dispersion of the IrO_2 and/or RuO_2 nanoparticles and therefore maximized surface area of the active phase. However, from a materials science point of view, the chemical and electrochemical stability of the OER catalyst supports are the primary challenge due to the high positive anode potential and the oxygen evolution environment. High specific surface area carbon and their nanostructured analogues e.g. carbon nanotubes are no longer applicable as the OER catalyst supports. The investigated materials are a few of oxides and ceramics e.g. SiC-Si[16], TiO_2[17] and SnO_2[18], Ti_nO_{2n-1}[19], TaC[14a], TiC[20] and antimony doped tin oxide[21-26]. Among these, antimony doped tin oxide has a wide range of applications such as water electrolysis[21], fuel cells[22], lithium-ion batteries,[23,24] solar cells[25] and gas sensors[26]. Antimony doped tin oxide could be a good alternative for OER catalyst supports, since it exhibits relatively high electronic conductivity and stability. Even though in an acidic medium and on long term polarisation at high anodic potentials, antimony doped tin oxide has much higher corrosion resistance and could hardly be oxidized electrochemically[27]. Except for the limitation of the support materials, sufficient charge transport[28], high specific surface area and preferable pore-size distribution[29] is also required to favor the availability of active phase.

At present, IrO_2 and/or RuO_2 supported on nanoparticle structured materials have been widely researched.[15, 30] Nanoparticle structured supports could be easily synthesized through simple sol-gel method[30a] or chemical co-precipitation method[14b], etc. The greatest advantages of nanoparticle structured supports are that high specific surface area could be obtained by optimization of the preparation method to refine the particle size. However, on the one hand, the tiny nanoparticle supported catalysts tend to aggregate in the preparation of the anode electrode or degrade the maintenance of their catalytic activity over the long term use under highly oxidizing conditions.[31] On the other hand, the nanoparticle supported catalysts could be wrapped by the added ionomers. Since the ionomers are electron resistant, the charge transfer rate may be decreased due to the hinder of ionomers, which resulting in decreasing of the electronic conductivity of the catalyst layers and leading to high ohmic overpotential.[32]

Fortunately, there are quite a few successful examples and theoretic predictions in other research filed that we can borrow to address the above issues. Very recently, one-dimensional (1-D) nanostructure materials such as nanowires and nanotubes have been considered as the most promising architectures to enhance the electrocatalytic activity.[33] Typically, the nanowire structured materials consisting of conductive oxide nanoparticles represent the advantages of the good charge transport properties[34], high surface areas[33] and preferable pore-size distribution.[35] The replacement of nanoparticle structure materials by new conducting 1-D nanostructure materials are of great interest as catalyst support materials.

In the present work, we explored the use of nanowire structured conductive oxide to support the active phase IrO_2. To the best of our knowledge, there were very few reports on the application of nanowire structured oxide supported catalysts in water electrolysis. We successfully introduced a new supported catalyst for OER by combining iridium oxide and antimony doped tin oxide nanowire. The antimony doped tin oxide nanowire was firstly synthesized via an electrospinning method, which was a facile and versatile process for producing webs of long and continuous metal oxide nanowires.[35b, 36] Finally, the supported IrO_2 catalysts were prepared and characterized with respect to the OER activity by electrochemical evaluation and tested in a PEM water electrolyzer. To elucidate the superior catalytic activity of the antimony doped tin oxide nanowire supported catalyst, antimony doped tin oxide nanoparticle had also been prepared by chemical co-precipitation method for comparison.[15b]

Experimental

Materials and methods

Chemicals

All the chemicals used in the present work were used as received without further purification. Nafion® solution (5 wt%) and Nafion® 212 were supplied by Dupont. $H_2IrCl_6{\cdot}H_2O$, PTFE emulsion (6 wt%) and 40 wt% Pt/C were received from Beijing Nonferrous Metal Research Institute, Shanghai Organic Fluorine Material Research Institute and Johnson Matthey, respectively. All other chemicals were purchased from Sinopharm Chemical Reagent Co. Ltd.

Synthesis of catalyst supports

The antimony doped tin oxide nanowires were prepared using the electrospinning method.[35b] Firstly, 3 g of Polyvinylpyrrolidone (PVP, Mw≈1300,000) was dissolved in 40 mL methanol under stirring. For antimony doped tin oxide precursor solution, 0.1 g of $SnCl_2{\cdot}2H_2O$ with 0.018 g of $SbCl_3{\cdot}2H_2O$ were dissolved in 40 mL methanol under stirring. The PVP and antimony doped tin oxide precursor solution were then mixed together. After the solution was loaded into a syringe that was part of the electrospinning setup, the solution was ejected into the multi-nozzle with a throughput of 1.2 ml h^{-1} for single-nozzle electrospinning systems. The metallic nozzles were connected to a high-voltage power supply (15 kV), and a rotating cage collector was placed 12 cm away from the tip of the multi-syringe needle. Referring to the TG-DSC curves (Fig S1), the as-spun antimony doped tin oxide nanowires precursor was firstly heated to 290 °C and kept at that temperature for 1 h to volatilize the moisture residual solvent in the precursors. The temperature was subsequently slowly increased to 450 °C and kept for 1h. This step allowed completely decompose the PVP to obtain the nanowire structure of antimony doped tin oxide. Finally, the

temperature was increased to 600 °C and held at that temperature for 4 h to crystallize the material. In the whole calcination process, a low heating rate of 0.5 °C min^{-1} was used to prevent the nanowire structure of antimony doped tin oxide from collapsing. The obtained support was referred to as Sb-SnO_2 NW. The antimony doped tin oxide nanoparticle was also prepared via a co-precipitation method reported in a previous work as a reference for comparison and hereafter was referred to Sb-SnO_2 NP.[15] It should be pointed out that the optimized Sb doping content of both the Sb-SnO_2 NW and Sb-SnO_2 NP is 5 mol% based on our previous work.[21]

Preparation of supported IrO_2 electrocatalysts

Modified Adams method was used to synthesize the supported IrO_2 catalysts.[18] The metal precursor $H_2IrCl_6 \cdot H_2O$, support powders (Sb-SnO_2 NW or Sb-SnO_2 NP) and $NaNO_3$ were first mixed in distilled water. The water was gradually evaporated by heating the mixture to 80 °C. The resulting salt mixture was collected and placed in a pre-heated muffle furnace and calcinated at 500 °C for 30 min. The fused salt-oxide mixture was then cooled down to 25 °C and washed with distilled water to remove the remaining salts. The IrO_2/Sb-SnO_2 NW (in mass ratio of 1:1) and IrO_2/Sb-SnO_2 NP (in mass ratio of 1:1) catalysts were finally obtained by drying at 80 °C in a vacuum oven for 12 h. Pure IrO_2 powders were also prepared using the same method as a reference for comparison.

Characterization

Thermogravimetric (TG) analysis was performed using a Netzsch STA 409 PC equipped with a Netzsch QMS 403 C mass spectrometer. Air was used as the purge gas and the samples were heated with a rate of 10 °C min^{-1}.

The crystalline structures of the prepared Sb-SnO_2 NW, Sb-SnO_2 NP were characterized by X-ray diffraction (XRD) using a Marcogroup diffractometer (MXP21 VAHF) with a Cu-Kα radiation source (λ=1.54056 Å) to characterize catalyst crystalline structure.

The micromorphology of the prepared Sb-SnO_2 NW, Sb-SnO_2 NP was studied using scanning electron microscopy (SEM) (ZEISS and LEO-1530 FESEM).

The physical surface area was determined by N_2 adsorption-desorption measurements (Micromeritics ASAP 2020, Micromeritics). Brunauer-Emmett-Teller (BET) formulations were used to calculate the surface area. Pore size distributions were estimated by applying the Barrett-Joyner-Halenda (BJH) method to the desorption branch of the isotherms.

Transmission electron microscopy (TEM) analysis was carried out with a Tecnai G2 F20 microscope operating at an accelerating voltage of 300 kV. The samples were first ultrasonically dispersed in ethanol for 10 minutes, and then a drop of the dispersion was deposited on a holey C/Cu TEM grid.

The conductivity measurement of the supports was operated according to a previously reported procedure.[15c] The samples were placed in a homemade stainless steel chamber with a PTFE inner sleeve (the conductivity cell) and pressed by two stainless steel pressure levers with a diameter of 10 mm. The pressure was firstly increased to 3 x 10^6 Pa for 60 s and then to 3 x 10^8 Pa. Measurements were performed at 25 °C in dry ambient atmosphere and the thickness of the pellet in the chamber was measured before and after the measurement by calipers. Electrochemical impedance spectroscopy was used for the conductivity measurement with frequency in a range of 1-10^6 Hz and ac amplitude of 10 mV.

For electrochemical evaluations, the catalyst powders were dispersed in isopropyl alcohol, into which Nafion® solution (5 wt%) and PTFE emulsion (6 wt%) was added. The mixtures were then homogenized for 1 h in an ice ultrasonic bath to form an ink. A 50 µL of the ink was pipetted on the surface of a glassy carbon working electrode with 7 mm diameter, followed by drying under a nitrogen atmosphere. For all the catalyst inks, the mass ratio of IrO_2 to Nafion® and PTFE was 14:2:1 and the loading of IrO_2 in the working electrode was 0.125 mg cm^{-2}. The electrochemical properties of the catalysts were characterized with a VMP2 electrochemical workstation by CV, EIS, and chronopotentiometry in a 0.5 mol L^{-1} H_2SO_4 solution at 25 °C. A Pt coil and a saturated calomel electrode (SCE) were used as the counter electrode and reference electrode, respectively. The potential window of CV was from 0 to 1 V vs. SCE using a scan rate from 2 to 300 mV s^{-1}. The EIS measurement was conducted at 1.25 V vs. SCE for the frequency between 5 mHz to 99 kHz with a sinus amplitude of 10 mV. The impedance data were modeled with ZSimpWin software. The polarization curves were acquired between 1.2 to 1.8 V vs. SCE with a scan rate of 1 mV s^{-1}.

Electrolyser cell test

An ink composed of the prepared catalysts, Nafion® solution, PTFE emulsion and isopropyl alcohol was sprayed on a PTFE sheet to form anode catalyst layer. After being dipped in the sodium chloride solution for 2 h and annealed at 340 °C for 30 min, the anode catalyst layer was dipped in 0.5 mol L^{-1} H_2SO_4 solution for 2 h and then in water for 2 h successively.[37] An ink composed of 40 wt% Pt/C as cathode catalyst, Nafion® solution and isopropyl alcohol was sprayed on a PTFE sheet to form cathode catalyst layer. The loading of IrO_2 was 0.75 mg cm^{-2} (determined gravimetrically within ±0.01 mg cm^{-2}) for the anode side and 0.2 mg cm^{-2} Pt for the cathode side.

Pretreatment of Nafion® 212 was accomplished by being successively treated in 5 wt% H_2O_2 solution, distilled water, 0.5 mol L^{-1} H_2SO_4 solution and distilled water at 80 °C and 60 min for each step. The catalyst coated membrane (CCM) was obtained by transferring the catalyst film from the PTFE film to the pretreated Nafion® 212 by the decal method under the conditions of 135 °C, 75 kg cm^{-2} for 3 min. The performance test was performed in a PEM electrolyser under ambient pressure at 80 °C. Membrane electrode assembly (MEA) (with a 1 cm^2 active area) was fabricated by placing the CCM between two carbon cloths. Distilled water was fed to the anode and cathode at a flow rate of 3 mL min^{-1}. The cathode of the cell was used as both the counter and reference electrode. Polarization curves were measured in constant current mode

by increasing the current density from 0 to 2 A cm^{-2}. As for the stability test under ambient pressure at 35 °C, the gas diffusion layers in the anode side were replaced for tantalum coated stainless steel felts.

Results and discussion

The schematic illustration of the synthetic route for the IrO_2/Sb-SnO_2 NW and IrO_2/Sb-SnO_2 NP is shown in Fig 1. Two different structured antimony doped tin oxides were selected for preparation of supported iridium oxide catalysts. The pore volume, surface area and electronic conductivity of the synthesized supports in the present work are summarized in Table 1.

For the as prepared Sb-SnO_2 NP, the electronic conductivity was 0.76 S cm^{-1} at 25 °C in ambient atmosphere. A slightly increase of the electronic conductivity for the as prepared Sb-SnO_2 NW was observed when the nanoparticles were assembled into nanowire structure, and the electronic conductivity of 0.83 S cm^{-1} was obtained at 25 °C in ambient atmosphere. It was a little higher than the values reported in the literatures, which were found to be of up to 10^{-1} S cm^{-1} level.[Error! Bookmark not defined.,38]

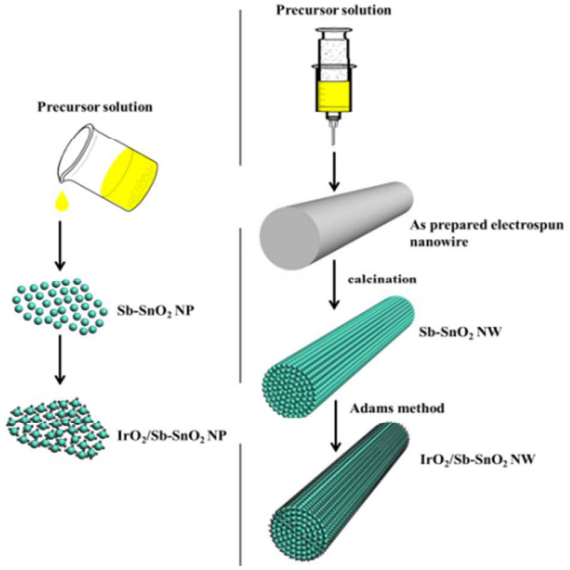

Fig 1 Schematic illustration of synthetic routes of IrO_2/Sb-SnO_2 NP and IrO_2/Sb-SnO_2 NW.

Table 1 Pore volumes, BET surface areas and conductivities of the synthesized supports.

	Pore volume (mL g^{-1})	Surface area (m^2 g^{-1})	Conductivity (S cm^{-1})
Sb-SnO_2 NW	0.191	60	0.83
Sb-SnO_2 NP	0.178	54	0.76

25 °C and without hydrates

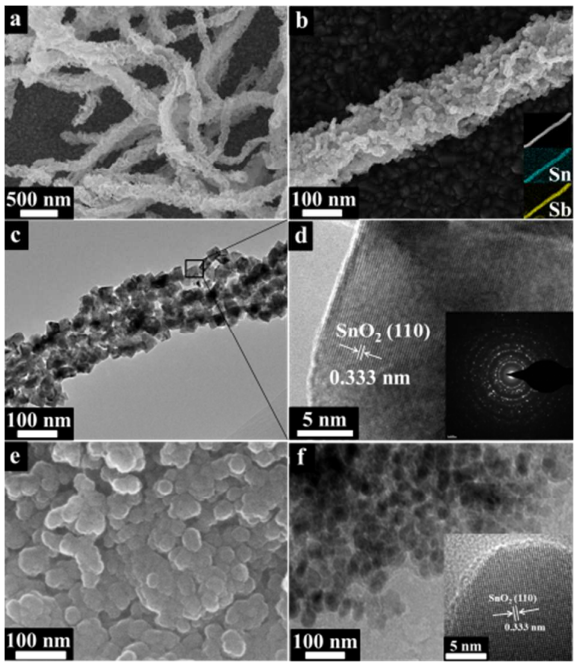

Fig 2 The low magnifying (a), high magnifying (b) SEM images (inset is SEM and the corresponding elemental mapping from EDX mapping image), TEM (c) images and HRTEM (d) images (inset is the corresponding selected-area electron diffraction (SAED) pattern) of Sb-SnO_2 NW, SEM (e) and TEM (f) images (inset is the corresponding HRTEM images) of Sb-SnO_2 NP.

Structural characterization

Fig 2 shows the microstructure of Sb-SnO_2 NW and Sb-SnO_2 NP. The as prepared Sb-SnO_2 NW (Fig 2a) exhibited continuous lengths of up to a few micrometers and uniform 1-D nanostructures (diameter: in the range of 200–300 nm). A magnified image (Fig 2b) revealed that the surface of thus prepared Sb-SnO_2 NW was rough at the nano-scale. Each nanowire had protrusions which consist primarily of fine Sb-SnO_2 nanoparticles. As shown in the elemental mapping from the EDX mapping image (inset in Fig 2b), both tin and antimony were observed in the same sample area. Antimony doping could give rise to enhance electrical conductivity of Sb-SnO_2 oxides.[38] The morphology and phase structure of the Sb-SnO_2 NW was further examined using transmission electron microscopy (TEM) of an individual Sb-SnO_2 NW. The nanowire structured Sb-SnO_2 was clearly demonstrated in Fig 2c, indicating that the Sb-SnO_2 NW was stacked from primary Sb-SnO_2 nanoparticles with diameters of 15-25 nm. As could be observed, the pore structure was formed and mainly caused by the gases produced from the decomposition of the organic material in the precursor. During the calcination process in air, the organic material was oxidized to gas. The produced gases diffused rapidly at the high temperature, which prevented the agglomeration of the Sb-SnO_2 particles.[36] The pore structure of Sb-SnO_2 NW was of importance for allowing easy access of the active surface sites to the electrolyte. Fig 2d shows the high resolution transmission electron microscopy (HRTEM) image of

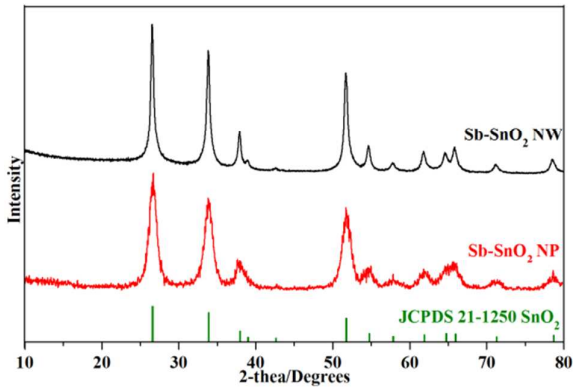

Fig 3 XRD patterns of Sb-SnO_2 NW support and Sb-SnO_2 NP support.

the synthesized Sb-SnO_2 NW, it revealed that the Sb-SnO_2 NW was crystalline rutile structures and showed the lattice fringes with the d spacing of 0.333 nm corresponding to the (110) lattice plane of tetragonal rutile SnO_2. Meanwhile, the selected area electron diffraction (inset in Fig 2d) showed that the electron diffraction pattern of the Sb-SnO_2 NW was composed of a series of concentric rings corresponding to the (110), (101) and (211) lattice planes, revealing the polycrystalline character of the Sb-SnO_2 NW. The morphologies and particle sizes of Sb-SnO_2 NP were investigated by SEM and TEM (Fig 2e and Fig 2f). As can be seen, the Sb-SnO_2 NP was in form of spheres within a diameter range of 40-50 nm, this was further confirmed by the TEM imaging. Moreover, the HRTEM image (inset in Fig 2f) of the Sb-SnO_2 NP demonstrated a fringe spacing of 0.333 nm, and this value agrees well with the spacing of the (110) lattice plane of tetragonal rutile SnO_2. On account of primary fine nanoparticles and thus fabricated pore structure of Sb-SnO_2 NW, the specific surface area and electrical conductivity slightly increased compared with Sb-SnO_2 NP.

X-ray diffraction patterns of the Sb-SnO_2 NW, Sb-SnO_2 NP were shown in Fig 3. The analysis of the diffraction data revealed that both of Sb-SnO_2 NW and Sb-SnO_2 NP possessed poly-crystalline structures and the patterns were matched well with the tetragonal rutile SnO_2 structure as indexed with the JCPDS 21-1250 file. This observation is corresponded well with the lattice fringes in the HRTEM micrograph (Fig 2d) and the SEAD pattern (inset in Fig 2d) above. Furthermore, no visible diffraction peaks of antimony oxide were observed for the samples, indicating that the antimony oxide entered the tin oxide lattice without formation of a second distinct phase.[39] However, one should take into account that the concentration of antimony oxide is less than 5% in the oxide phase. On the other hand, Wang et al. have reported no structural changes in the SnO_2 lattice when up to 15 mol% antimony was accommodated.[40]

Fig 4 shows the N_2 adsorption/desorption isotherms of the Sb-SnO_2 NW and Sb-SnO_2 NP. As shown in Fig 4, the corresponding BJH pore size distribution analysis based on the desorption branch (inset in Fig 4) showed that the Sb-SnO_2 NW exhibited relatively uniform mesopores centred at around

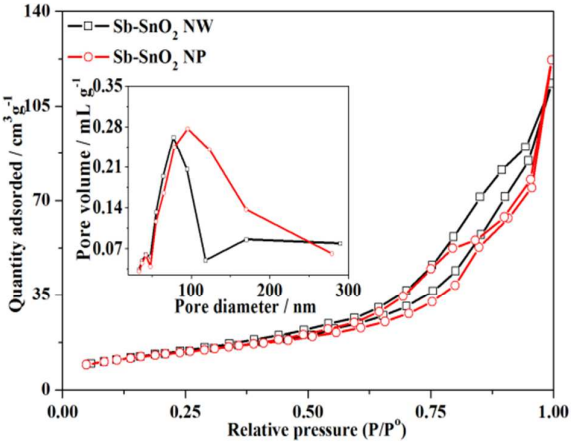

Fig 4 shows the N_2 adsorption/desorption isotherms.

75 nm, while the Sb-SnO_2 NP contained less uniform mesopores with diameters spanning a range from 30 nm to 250 nm. The calculated pore volumes and surface areas are summarized in Table 1. The pore volume and BET surface area of Sb-SnO_2 NW was 0.191 cm^3 g^{-1} and 60 $m^2 g^{-1}$, respectively. While, the pore volume and BET surface area of Sb-SnO_2 NP was 0.178 cm^3 g^{-1} and 54 m^2 g^{-1}, respectively, which were slightly lower than those of Sb-SnO_2 NW.

As seen from above, the Sb-SnO_2 NW could be viewed as assembling Sb-SnO_2 nanoparticles together randomly into nanowire structure via a simple and effective electrospinning method. The structural improvement of Sb-SnO_2 NW contributed to tiny beneficial effects on the specific surface area and the electronic conductivity except for more uniform pore size distribution compared with Sb-SnO_2 NP. However, the Sb-SnO_2 NW was designed to support active phase IrO_2 for OER catalyst. The characteristic nanowire structure and the fabricated pore structure of the support were expected to promote the charge transport in the catalyst layer, as to be discussed below.

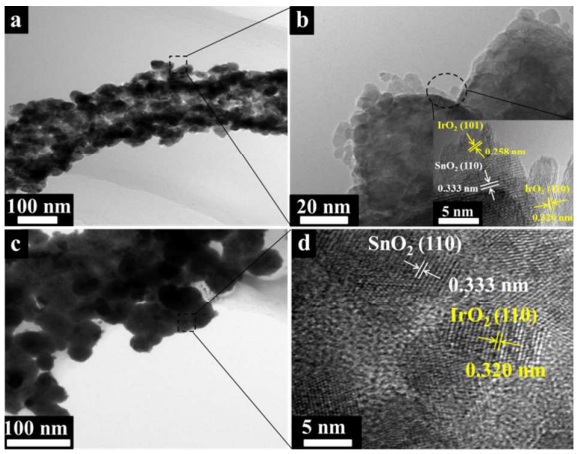

Fig 5 The low magnifying (a), high magnifying (b) TEM images (inset is the corresponding HRTEM) of IrO_2/Sb-SnO_2 NW, TEM (a) images and the HRTEM (b) images of IrO_2/Sb-SnO_2 NP.

Fig 5 shows the TEM and HRTEM images of the synthesized IrO_2 catalysts using Sb-SnO_2 NW and Sb-SnO_2 NP as supports. Both the TEM image (Fig 5a and Fig 5c) and the SEM image (Fig S2a and Fig S2b) of the as-prepared catalysts showed that, after the IrO_2 nanoparticles were loaded on the different supports, the corresponding catalysts maintained the original structure of the supports, respectively. As shown in Fig 5b, it appeared that the small and uniformly distributed IrO_2 nanoparticles (5-8 nm diameter) were well adhered to the Sb-SnO_2 NW support. The HRTEM images of IrO_2/Sb-SnO_2 NW (inset in Fig 5b) and IrO_2/Sb-SnO_2 NP (Fig 5d) showed the lattice fringes with distinct d spacing of IrO_2 (0.320 nm and 0.258 nm) and SnO_2 (0.333 nm) corresponding to those of the IrO_2(110) plane, IrO_2(101) plane and SnO_2 (110) plane, respectively. The elemental mapping (inset in Fig S2a) of the IrO_2 phase (Ir in red), the Sb-SnO_2 phase (Sn in pink) and the elemental composition of the supported catalysts (Fig S2c and Fig S2d) were also verified by using EDX analysis, and the results confirmed that the IrO_2 phases were present for both catalysts. We further examined the crystalline structures of the supported catalyst by means of a XRD analysis (Fig S3), which indicated that IrO_2/Sb-SnO_2 NW and IrO_2/Sb-SnO_2 NP samples were properly formed without any impurity phase.

Electrochemical characterization

To evaluate the catalytic activity of the prepared catalysts, the mass specific activity based on the IrO_2 loading of 0.125 mg cm^{-2} was used in the following discussion. Cyclic voltammetry in double electrode layer region was used to characterize the electrochemical behavior of prepared catalysts. Fig 6a shows the representative cyclic voltammograms (CVs) of IrO_2/Sb-SnO_2 NW, IrO_2/Sb-SnO_2 NP, IrO_2 catalysts, Sb-SnO_2 NW and the bare glass carbon substrate at a scan rate of 10 mV s^{-1} in N_2-saturated 0.5 mol L^{-1} H_2SO_4 at 25 °C. As shown in Fig 6a, the capacitance of Sb-SnO_2 NW support and the bare glass carbon substrate is nearly negligible as compared with that of the prepared catalysts. The CVs of each catalyst exhibited the typical pseudo capacitive behavior with a broad redox peak which could be attributed to the reversible oxidation and reduction on the IrO_2 surface. From the CVs, an integration of the voltammogram between 0 and 1 V vs. SCE for the forward sweep was made to obtain the anode voltammetric charge, which previously was proposed to be related to the active surface areas of different catalysts.[15,21]

Fig 6b showed the voltammetric charges for each catalyst obtained at different potential scan rate. It could be seen that the charges increased slightly with decreasing scanning rates especially at the lower scanning rates. According to Ardizzone[41,42] and Trasatti[43], two kinds of information of the electrochemically active surface area of metal oxide electrodes, the "outer" voltammetric charge (Q_o) and the total voltammetric charge (Q_t), could be obtained as the scan rate approaches to the zero scan rate[18b]. At very high scanning rates, proton exchange took place only on more accessible "outer" active surface, but occurred on the total active surface (both the "outer" and less accessible "inner" surfaces) at very low potential scan rates. Correspondingly, the former (Q_o) related to the "outer" active surface was that directly exposed to the electrolyte, and the voltammetric charge (Q_t-Q_o) normally related to less accessible "inner" surfaces was that proton exchange took place relying on proton diffusion. The ratio of Q_o/Q_t was therefore associated with the proton diffusion into subsurface regions through pores, cracks, etc., which depended on the porosity and particles wrapped by the proton conducting phase.

The obtained total charge, outer charge and charge ratio of all the prepared catalysts were investigated and are summarized in Table 2. Compared with IrO_2, an obvious increase of the total charge, or in other words, the number of the catalytically active sites was observed as well as an increase of Q_o/Q_t ratio for IrO_2/Sb-SnO_2 NP. It could possibly be attributed to the better dispersion of the iridium oxide particles on Sb-SnO_2 NP. A more significant improvement in the catalytically active sites was achieved when IrO_2 was supported on Sb-SnO_2 NW. From the above BET surface area and conductivity test, the structural improvement of Sb-SnO_2 NW contributed to tiny beneficial effects on the specific surface area as well as the electronic conductivity. Thus, for the IrO_2/Sb-SnO_2 NW, the increase of the catalytically active sites might be attributed to the synergistic effect of the nanowire structure and preferable pore-size distribution of the support. This could be further confirmed by the evidence of enhanced Q_o/Q_t ratio for IrO_2/Sb-SnO_2 NW compared with IrO_2/Sb-SnO_2 NP. It should be pointed that the limited Q_o/Q_t ratio indicated that the charging process was limited by the slow proton diffusion. For IrO_2/Sb-SnO_2 NW, the nanowire structure of Sb-SnO_2 NW not only ensured that the active phase was well distributed, but also provided sufficient charge pathways required in the subsurface regions (as discussed in Fig 6c). Furthermore, the fabricated pore structure of the support could provide more accessible surface area for the electrolyte and accelerate the release of oxygen gas, which could facilitate the availability of active phase.

The charge transfer resistance is in fact of significance to OER activity of the supported catalysts. To shed light the charge transport properties afforded by support with different structures of the prepared catalysts, EIS characterization was carried out for the Sb-SnO_2 NW, Sb-SnO_2 NP supported IrO_2 catalysts, and pure IrO_2, respectively at 1.25 V vs. SCE, which corresponded to the oxygen evolution region. Fig 6c showed the EIS measurement in Nyquist plots and an appropriate equivalent electrical circle (EEC) shown in the inset of Fig 6c was selected to fit the impedance data. Among where R_Ω was the ohmic resistance of working electrode and electrolyte between working electrode and reference electrode, R_{ct} was the charge transfer resistance of a faradic process occurring at the oxide/electrolyte interface, which was a measure of the polarization resistance or the catalytic activity of the electrode and was directly related to the OER kinetics.[44] The impendence parameters for IrO_2/Sb-SnO_2 NW, IrO_2/Sb-SnO_2 NP and IrO_2 were described in Table 2. As seen from Table 2, the R_{ct} was decreased immensely from 3.415 ohm cm^2 for IrO_2 and 1.710 ohm cm^2 for IrO_2/Sb-SnO_2 NP to 0.812 ohm cm^2 for IrO_2/Sb-

SnO_2 NW, and the IrO_2/Sb-SnO_2 NW exhibited significantly lowest R_{ct} than that of pure IrO_2 and IrO_2/Sb-SnO_2 NP. It is speculated that the characteristic nanowire structure and the fabricated pore structure of the Sb-SnO_2 NW could enhance charge transport properties during the OER reactions. As for the R_{ohm}, it should be remarked that the loading of the catalyst on the glassy carbon electrode is relatively low. Better electron conductivity of the pure IrO_2 than that of Sb-SnO_2 resulted in less ohmic resistance (R_{ohm}). While, slightly lower R_{ohm} of IrO_2/Sb-SnO_2 NW was obtained than that of IrO_2/Sb-SnO_2 NP, which was consistent with the conductivity test of different support.

The effect of catalyst supports with different structure on the catalytic activity of IrO_2 was further examined by steady state polarization curves of catalysts recorded in the potential region for the oxygen evolution reactions. For comparison, the polarization curves of Sb-SnO_2 NW and the bare glass carbon substrate were also recorded. The polarization curves of Sb-SnO_2 NW and the bare glass carbon substrate showed weak current densities within the test potential region (Fig 6d), and it could be concluded that the Sb-SnO_2 materials contributed negligible catalytic activity toward the OER. While the anodic current density of the prepared catalysts increased with the increase of the applied potential. As listed in Table 2, to reach a current density of 10 mA cm^{-2}, the overpotentials η (against the thermodynamic equilibrium potential of OER, 1.23 V) of IrO_2/Sb-SnO_2 NW, IrO_2/Sb-SnO_2 NP and IrO_2 were measured to be 0.008 V vs. SCE, 0.030 V vs. SCE and 0.043 V vs. SCE, respectively. It should be pointed that the loading of IrO_2 in all test electrodes was 0.125 mg cm^{-2}, indicating that the IrO_2/Sb-SnO_2 NW showed the best electrocatalytic performance on mass activity, and it was further proved from the mass normalized polarization curves of the catalysts (Fig S4). It showed that Sb-SnO_2 NW support could help the dispersion of the active component and enhanced the catalyst efficiency. However, a problem in the enhancement of the mass activity of the IrO_2/Sb-SnO_2 NW was the separation of electronic effects (intrinsic activity) from geometric effects (related to catalytically active areas only). According to the previous literatures [45], normalizing the measured currents with the corresponding total charge could represent intrinsic activity of the corresponding materials. Thus obtained intrinsic activity of IrO_2/Sb-SnO_2 NW was almost identical with the pure IrO_2 (Fig S5) at low current density. According to Rozain and Millet[46], at low current density, in the so-called activation governed potential region, the current-voltage relationship was controlled by the OER kinetics, and this potential region was used to evaluate the intrinsic activity of the catalyst. It could be concluded that the IrO_2/Sb-SnO_2 NW outperformed the IrO_2 in the mass activity may be mainly attributed to the improvement of catalytically active sites. Due to the negligible catalytic activity toward the OER of the Sb-SnO_2 materials, the higher mass activity of the IrO_2/Sb-SnO_2 NW than that of IrO_2 could be attributed to the better dispersion of the iridium oxide particles on the supports. Compared with the Sb-SnO_2 NP, although the physical surface area of the Sb-SnO_2 NW was not promoted substantially, higher mass activity might be contributed to the porous nanowire structure, which provide an open structure with appropriate pore-size distribution and enhanced charge transport properties. Fig S6 and Table 2 summarized the corresponding Tafel slopes of the catalysts for evaluating the catalytic kinetics of the catalysts towards the OER. At the applied overpotential ranges, the measured Tafel slopes of the catalysts were around 60 mV dec^{-1}, which were in agreement with literature datas for pure IrO_2 and exhibited the similar reaction mechanism.[47] It should be noted that both the Tafel slopes of IrO_2/Sb-SnO_2 NW and IrO_2/Sb-SnO_2 NP were slightly lower than that of IrO_2, and better OER kinetics were probably related to a possible specific interaction between IrO_2 and Sb-SnO_2. As suggested in previous reports,[18a,48] SnO_2 could facilitate the removal of adsorbed hydroxy species and increase the utilization ratio of the active phase.

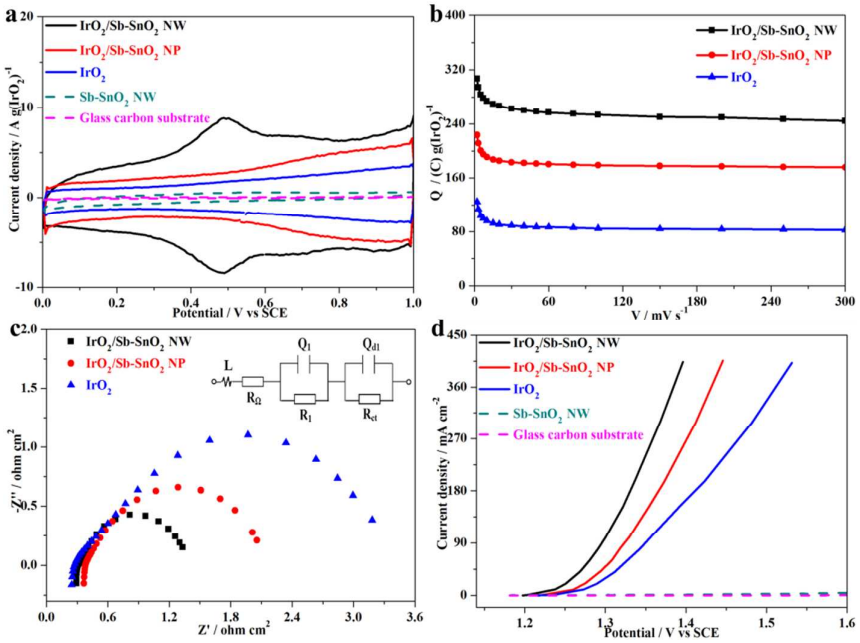

Fig 6 (a) Representative CVs recorded with a scan rate of 10 mV s^{-1}, (b) Charge as functions of scan rate for IrO_2/Sb-SnO_2 NW, IrO_2/Sb-SnO_2 NP and IrO_2, (c) Nyquist diagram of three types of prepared catalysts measured at 1.25 V vs. SCE during oxygen evolution, the inset was equivalent circuit, (d) Steady-state polarization curves of the three types of prepared catalysts at scan rate of 1 mV s^{-1}. All the electrochemical characterization is tested in the 0.5 mol L^{-1} H_2SO_4 at 25 °C.

Table 2 Summary of electrochemical characterization of prepared catalysts.

	CV			EIS		Overpotentials	Tafel slopes
	$Q_t^{(a)}$	$Q_o^{(a)}$	$Q_o/Q_t^{(a)}$	$R_{ohm}^{(b)}$	$R_{ct}^{(b)}$	$\eta^{(c)}$	$S^{(d)}$
IrO_2	105	71	0.676	0.216	3.415	0.043	66
IrO_2/Sb-SnO_2 NP	200	166	0.831	0.374	1.710	0.030	56
IrO_2/Sb-SnO_2 NW	286	246	0.860	0.277	0.812	0.008	54

(a) Total charge (Q_t / C (g-IrO_2)$^{-1}$), outer charge (Q_o / C (g-IrO_2)$^{-1}$) and charge ratio (Q_o/Q_t) of all prepared catalysts calculated from the cyclic voltammograms. (b) Ohmic resistance (R_{ohm} / ohm cm^2), charge-transfer resistance (R_{ct} / ohm cm^2). (c) Overpotentials (η / V vs. SCE). (d) Tafel slopes (S / mV dec^{-1}).

Single cell performance

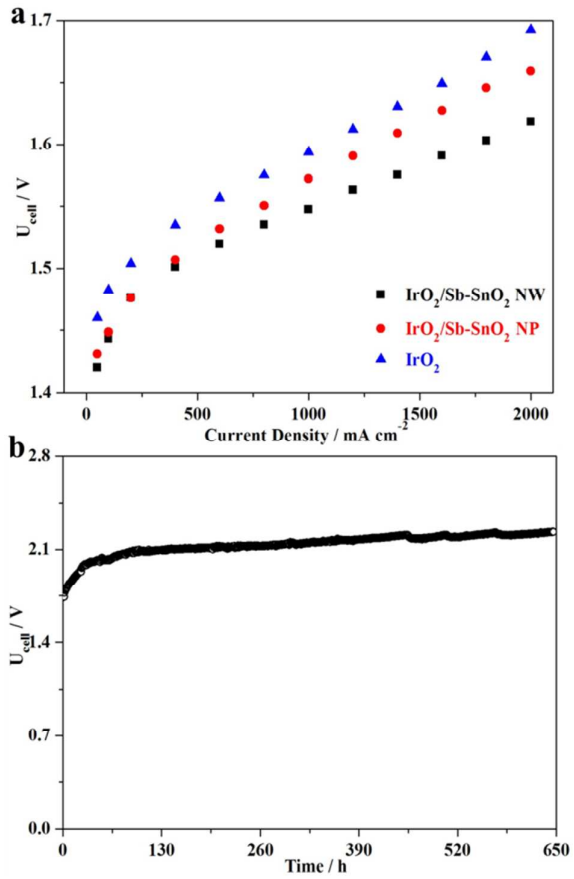

Fig 7 (a) Current-voltage curves of PEM water electrolysis cells with different anode catalysts operating at 80 °C with Nafion® 212 membrane. The operational pressure was ambient and the cathode was made of 40 wt% Pt/C with a Pt loading of 0.2 mg cm^{-2}, (b) Stability of PEM water electrolysis cells operating at temperature of 35 °C and current density of 450 mA cm^{-2} under atmospheric pressure. The anode consisted of IrO_2/Sb-SnO_2 NW catalyst at an IrO_2 loading of 0.75 mg cm^{-2} and the cathode was made of 40 wt% Pt/C at a Pt loading of 0.2 mg cm^{-2}.

By using a Nafion® 212 membrane as an electrolyte, MEAs based on IrO_2, IrO_2/Sb-SnO_2 NP, IrO_2/Sb-SnO_2 NW anodes and a cathode with 40% Pt/C as a catalyst were prepared and tested in a homemade electrolyser.[15c,32] In the present study, the cathode catalyst, loading and fabrication process remained unchanged in order to investigate the effect of anode catalysts with different supports. As seen from Fig 7a, the electrolysis cell performance operated at 80 °C under ambient pressure was steadily improved in the order: IrO_2 < IrO_2/Sb-SnO_2 NP < IrO_2/Sb-SnO_2 NW. No sign of transport hindrance was observed up to a current density of 2 A cm^{-2}. Therefore, the huge disparity in the performance was mainly because of ohmic resistance and the polarization resistance. Due to the better dispersion of iridium oxide on the Sb-SnO_2 NP and therefore the increased number of active sites, the performance of IrO_2/Sb-SnO_2 NP was improved compared with pure IrO_2 catalyst. For IrO_2/Sb-SnO_2 NW, A more significant improvement in the performance was achieved, which could be attributed to the improvement of the conductivity in the catalyst layers primarily due to the enhanced charge transport properties afforded by the Sb-doped SnO_2 nanowires support. The terminal voltage of electrolysis cell of MEA prepared with IrO_2/Sb-SnO_2 NW catalyst was 1.62 V at current density of 2 A cm^{-2}. It should be remarked that the electrodes were prepared by spraying the ultrasonic inks and then hot-pressed on the polymer membranes. During the procedure, the nanowire structure of the catalysts might be damaged to some extent. However, the performance was considerably improved, indicating the remaining effect of the nanowire structure of the support.

The durability of the electrolyser performance is one of the critical concerns for characterizations of materials and components. To evaluate the stability of the IrO_2/Sb-SnO_2 NW catalyst, an electrolysis cell was tested under a constant current density of 450 mA cm^{-2} at 35 °C. As shown in Fig 7b, the cell presented reasonably good stability for 646 h and the degradation rate of cell voltage was about 0.76 mV h^{-1}. During the initial 90 hours, the voltage had a sharp increase from 1.73 to 2.09 V. It could be caused by the fact that the blocking of membrane exchanging sites by some metal cations and resulted in increasing the electrochemical overpotential[49]. After stabilization period of the initial 90 h, the cell presented reasonably good stability for 556 h. In brief, the electrolyzer

test confirmed high activity and stability for the supported catalysts. It should be noted that in terms of catalyst evaluation, comparison of the water electrolysis performance and stability with literature results is by no means straightforward, as membranes, electrode structures and cell assemblies are also playing a role. Moreover no systematic efforts were made to optimize the catalyst ink and hot-pressing procedure for the MEA fabrication, which could be expected to further improve both the cell performance and stability.

Conclusions

In summary, we rationally developed a novel catalyst support with functionalities of nanowire structure and pore structure via a simple and effective electrospinning method from antimony doped tin oxide. Compared with Sb-SnO_2 NP, the pore volume, BET surface area and electronic conductivity of Sb-SnO_2 NW were slightly increased. However, the structural improvement of Sb-SnO_2 NW contributed to more uniform pore size distribution and enhanced charge transport properties. The catalyst activity of Sb-SnO_2 NW supported iridium oxide catalyst toward the OER was investigated and showed about three times higher catalytic activity than that of the pure IrO_2 catalyst. The good catalytic activity was further confirmed by electrolyser test operated at 80 °C, and the terminal voltage was 1.62 V at 2 A cm^{-2} with an IrO_2 loading of 0.75 mg cm^{-2}, a Pt loading of 0.2 mg cm^{-2}. At 35 °C and 450 mA cm^{-2} the cell showed good stability with a period of 646 hours.

Acknowledgements

Financial support for this work is acknowledged from the 863 Program of China (Project no. 2012AA053401), the National Natural Science Foundation of China (Grant no. 51274028).

Notes and reference

1 (a) S. Park, Y. Y. Shao, J. Liu and Y. Wang, *Energy Environ. Sci.*, 2012, 5, 9331; (b) M. Balat and H. Balat, *Energy Sources, Part A*, 2009, 31, 1280; (c) T. R. Cook, D. K. Dogutan, S. Y. Reece, Y. Surendranath, T. S. Teets and D. G. Nocera, *Chem. Rev.*, 2010, 110, 6474.

2 (a) H. Dau, C. Limberg, M. Rish, M. Roggan, T. Reier and P. Strasser, ChemCatChem, 2010, 2, 724; (b) D. V. Esposito, S. T. Hunt, A. L. Stottlemyer, K. D. Dobson, B. E. McCandless, R. W. Birkmire and J. G. Chen, *Angew. Chem., Int. Ed.*, 2010, 49, 9859; (c) D. Merki and X. L. Hu, *Energy Environ. Sci.*, 2011, 4, 3878; (d) S. A. Grigoriev, V. I. Porembsky and V. N. Fateev, *Int. J. Hydrogen Energy*, 2006, 31, 171.

3 (a) E. Fabbri, A. Habereder, K. Waltar, R. Kötza and T. J. Schmidt, Catal. Sci. & Technol., 2014, 4, 3800; (b) I. C. Man, H. Y. Su, F. CalleVallejo, H. A. Hansen, J. I. Martínez, N. G. Inoglu, J. Kitchin, T. F. Jaramillo, J. K. Nørskov and J. Rossmeisl, *ChemCatChem*, 2011, 3, 1159.

4 J. K. Nørskov, J. Rossmeisl, A. Logadottir, L. Lindqvist, J. R. Kitchin, T. Bligaard and H. Jonsson, *J. Phys. Chem. B*, 2004, 108, 17886.

5 S. Trasatti, Electrocatalysis: understanding the success of DSA, *Electrochim. Acta*, 2000, 45, 2377.

6 A. Marshall, B. Børresen, G. Hagen, M. Tsypkin and R. Tunold, *Mater. Chem. Phys.*, 2005, 94, 226.

7 (a) J. Aromaa and O. Fors´en, *Electrochim. Acta*, 2006, 51, 6104; (b) R. S. Yeo, J. Orehotsky, W. Visscher and S. Srinivasan, *J. Electrochem. Soc.*, 1981, 128, 1900.

8 (a) X. M. Wang, J. M. Hu and J. Q. Zhang, *Electrochim. Acta*, 2010, 55, 4587; (b) J. J. Zhang, J. M. Hu, J. Q. Zhang and C. N. Cao, *Int. J. Hydrogen Energy*, 2011, 36, 5218.

9 Z. G. Ye, H. M. Meng, D. Chen, H. Y. Yu, Z. S. Huan, X. D. Wang and D. B. Sun, *Solid State Sci.*, 2008, 10, 346.

10 (a) L. M. Da Silva, J. F. C. Boodts and L. A. De Faria, *Electrochim. Acta*, 2001, 46, 1369; (b) M. V. Makarova, J. Jirkovsk´y, M. Klementov´a, I. Jirka, K. Macounov´a and P. Krtil, *Electrochim. Acta*, 2008, 53, 2656.

11 (a) M. H. P. Santana and L. A. De Faria, *Electrochim. Acta*, 2006, 51, 3578; (b) M. H. P. Santana, L. M. Da Silva and L. A. De Faria, *Electrochim. Acta*, 2003, 48, 1885.

12 (a) S. Ardizzone, C. L. Bianchi, G. Cappelletti, M. Ionita, A. Minguzzi, S. Rondinini and A. Vertova, *J. Electroanal. Chem.*, 2006, 589, 160; (b) L. K. Xu, Y. L. Xin and J. T. Wang, *Electrochim. Acta*, 2009, 54, 1820.

13 J. B. Cheng, H. M. Zhang, H. P. Ma, H. X. Zhong and Y. Zou, *Int. J. Hydrogen Energy*, 2009, 34, 6609.

14 (a) J. Polonsky´, I. M. Petrushina, E. Christensen, K. Bouzek, C. B. Prag, J. E. T. Andersen and N. J. Bjerrum, *Int. J. Hydrogen Energy*, 2012, 37, 2173; (b) R. Borup, J. Meyers, B. Pivovar, Y. S. Kim, R. Mukundan, N. Garland, D. Myers, M. Wilson, F. Garzon, D. Wood, P. Zelenay, K. More, K. Stroh, T. Zawodzinski, J. Boncella, J. E. McGrath, M. Inaba, K. Miyatake, M. Hori, K. Ota, Z. Ogumi, S. Miyata, A. Nishikata, Z. Siroma, Y. Uchimoto, K. Yasuda, K. I. Kimijima and N. Iwashita, *Chem. Rev.*, 2007, 107, 3904; (c) Y. Shao, J. Liu, Y. Wang and Y. Lin, *J. Mater. Chem.*, 2009, 19, 46.

15 (a) X. Wu and K. Scott, *Int. J. Hydrogen Energy*, 2011, 36, 5806; (b) J. Y. Xu, D. Aili, Q. F. Li, E. Christensen, J. O. Jensen, W. Zhang, M. K. Hansen, G. Y. Liu, X. D. Wang and N. J. Bjerrum, *Energy Environ. Sci.*, 2014, 7, 820; (c) G. Y. Liu, J. Y. Xu, J. M. Jiang, B. S. Peng and X. D. Wang, *Int. J. Hydrogen Energy*, 2014, 39, 1914.

16 A. V. Nikiforov, A. L. Tomás García, I. M. Petrushina, E. Christensen and N. J. Bjerrum, *Int. J. Hydrogen Energy*, 2011, 36, 5797.

17 P. Mazúr, J. Polonský, M. Paidar and K. Bouzek, *Int. J. Hydrogen Energy*, 2012, 37, 12081.

18 (a) J. Y. Xu, G. Y. Liu, J. L. Li and X. D. Wang, *Electrochim. Acta*, 2012, 59, 105; (b) J. Y. Xu, Q. F. Li, E. Christensen, X. D. Wang and N. J. Bjerrum, *Int. J. Electrochem. Sci.*, 2013, 8, 2388.

19 S. Siracusano, V. Baglio, C. D'Urso, V. Antonucci and A. S. Aricò, *Electrochim. Acta*, 2009, 54, 6292.

20 L. R. Ma, S. Sui and Y. C. Zhai, *J. Power Sources*, 2008, 177, 470.

21 J. Y. Xu, Q. F. Li, M. K. Hansen, E. Christensen, A. L. Tomás-García, G. Y. Liu, X. D. Wang and N. J. Bjerrum, *Int. J. Hydrogen Energy*, 2012, 24, 18629.
22 K. S. Lee, I. S. Park, Y. H. Cho, D. S. Jung, N. Jung and H. Y. Park, *J. Catal.*, 2008, 258, 143.
23 Y. D. Wang, I. Djerdj, B. Smarsly and M. Antonietti, *Chem. Mater.*, 2009, 21, 3202.
24 F. D. Wu, M. H. Wu and Y. Wang, *Electrochem. Commun.*, 2011, 13, 433.
25 Y. S. Kim, B. K. Yu, D. Y. Kim and W. B. Kim, *Sol. Energy Mater. Sol. Cells*, 2011, 95, 2874.
26 V. M. Aroutiounian, A. Z. Adamyan, E. A. Khachaturyana, Z. N. Adamyan, K. Hernadi and Z. Pallai, *Sens. Actuators B*, 2013, 177, 308.
27 V. K. Puthiyapura, M. Mamlouk, S. Pasupathi, B. G. Pollet and K. Scott, *J. Power Sources*, 2014, 269, 451.
28 V. Müller, M. Rasp, G. Štefanić, J. H. Ba, S. Günther and J. Rathousky, *Chem. Mater.*, 2009, 21, 5229.
29 (a) A. Marshall, B. Børresen, G. Hagen, M. Tsypkin and R. Tunold, *Electrochim. Acta*, 2006, 51, 3161; (b) X. W. Yu, M. Zhang, W. J. Yuan and G. Q. Shi, *J. Mater. Chem. A,* 2015, 3, 6921.
30 (a) T. Ioroi, N. Kitazawa, K. Yasuda, Y. Yamamoto and H. Takenaka, *J. Appl. Electrochem.*, 2001, 31, 1179; (b) S. Y. Huang, P. Ganesan, H. Y. Jung and B. N. Popov, *J. Power Sources*, 2012, 198, 23.
31 (a) P. J. Ferreira, G. J. la O', Y. Shao-Horn, D. Morgan, R. Makharia, S. Kocha and H. A. Gasteiger, *J. Electrochem. Soc.*, 2005, 152, A2256; (b) Y. Shao-Horn, W. C. Sheng, S. Chen, P. J. Ferreira, E. F. Holby and D. Morgan, *Top. Catal.*, 2007, 46, 285.
32 G. Y. Liu, J. Y. Xu, Y. T. Wang, J. M. Jiang and X. D. Wang, *Int. J. Hydrogen Energy*, 2014, 39, 14531.
33 (a) C. L. Zhang and S. H. Yu, *Chem. Soc. Rev.*, 2014, 43, 4423; (b) S. M. Bergin, Y. H. Chen, A. R. Rathmell, P. Charbonneau, Z. Y. Li and B. J. Wiley, *Nanoscale*, 2012, 4, 1996.
34 Y. Xia, P. Yang, Y. Sun, Y. Wu, B. Mayers, B. Gates, Y. Yin, F. Kim and H. Yan, *Adv. Mater.*, 2003, 15, 353.
35 (a) S. Chauhan, G. J. Richards, T. Mori, P. F. Yan, J. P. Hill, K. Ariga, J. Zou and J. Drennan, *J. Mater. Chem. A*, 2013, 1, 6262; (b) Y. S. Kim, H. S. Jang and W. B. Kim, *J. Mater. Chem.*, 2010, 20, 7859.
36 (a) S. J. Choi, B. H. Jang, S. J. Lee, B. K. Min, A. Rothschild, and I. D. Kim, *Appl. Mater. Interfaces*, 2014, 6, 2588; (b) S. Jiang, B. Zhao, R. Ran, R. Cai, M. O. Tad´e and Z. P. Shao, *RSC Adv.*, 2014, 4, 9367.
37 J. Y. Xu, R. Y. Miao, T. T. Zhao, J. Wu and X. D. Wang, *Electrochem. Commun.*, 2011, 13, 437.
38 (a) T. N¨utz, U. Z. Felde and M. Haase, *J. Chem. Phys.*, 1999, 110, 12142; (b) C. Goebbert, M. A. Aegerter, D. Burgard, R. Nass and H. Schmidt, *J. Mater. Chem.*, 1999, 9, 253; (c) Y. H. Hu, H. H. Zhang and H. M. Yang, *J. Alloys Compd.*, 2008, 453, 292.
39 (a) J. Kong, H. Deng, P. Yang and J. Chu, *Mat. Chem. Phys.*, 2009, 114, 854; (b) X. Zhong, B. Yang, X. Zhang, J. Jia and G. Yi, *Particuology*, 2012, 10, 365.
40 Y. D. Wang and T. Cheng, *Electrochim. Acta*, 2009, 54, 3510.
41 S. Ardizzone, G. Fregonara and S. Trasatti, *Electrochim Acta*, 1990, 35, 263.
42 G. Spinolo, S. Ardizzone and S. Trasatti, *J. Electroanal. Chem.*, 1997, 423, 49.
43 C. P. De Pauli and S. Trasatti, *J. Electroanal. Chem.*, 1995, 396, 161.
44 (a) J. M. Hu, J. Q. Zhang and C. N. Cao, *Int. J. Hydrogen Energy*, 2004, 29, 791; (b) T. A. F. Lassali, J. F. C. Boodts and L. O. S. Buohões, *Electrochim. Acta*, 1999, 44, 4203.
45 (a) W. Hu, Y. Q. Wang, X. H. Hu, Y. Q. Zhou and S. L. Chen, *J. Mater. Chem.*, 2012, 22, 6010; (b) C.P. De Pauli and S. Trasatti, *J. Electroanal. Chem.*, 2002, 538-539, 145; (c) J. J. Zhang, J. M. Hu, J. Q. Zhang and C. N. Cao, *Int. J. Hydrogen Energy*, 2011, 36, 5218.
46 C. Rozain and P. Millet, *Electrochim. Acta*, 2014, 131, 160.
47 (a) J. Rossmeisl, Z. W. Qu, H. Zhu, G. J. Kroes and J. K. Nørskov, *J. Electroanal. Chem.*, 2007, 607, 83; (b) M. E. G. Lyons and S. Floquet, *Phys. Chem. Chem. Phys.*, 2011, 13, 5314; (c) A. S. Kelsey, Q. Liang, D. B. Michael, and S. H. Yang, *J. Phys. Chem. Lett.*, 2014, 5, 1636.
48 F. Sergio, R. Davide and A. M. Carlos, *Electrochim. Acta*, 2014, 146, 257.
49 G. Q. Wei, Y. X. Wang, C. D. Huang, Q. J. Gao, Z. T. Wang and L. Xu, *Int. J. Hydrogen Energy*, 2010, 35, 3951.

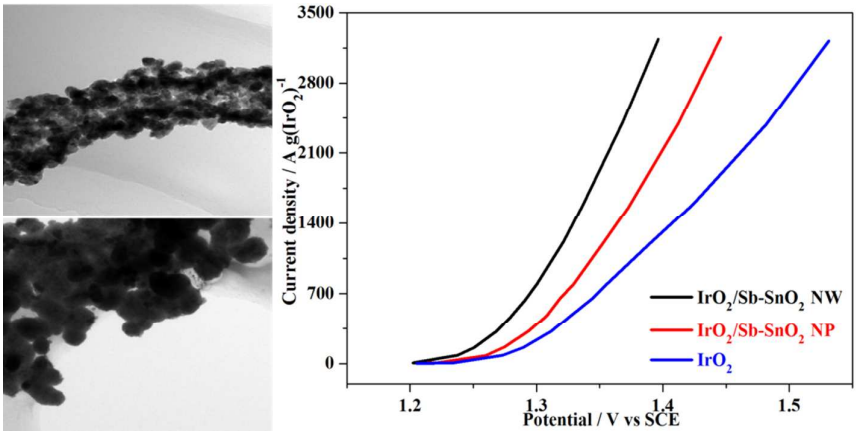

Porous Sb-SnO_2 nanowires synthesized as support for IrO_2 by electrospinning method. Thus prepared catalyst exhibits enhanced mass activity toward OER.